

Spectroscopy with the Engineering Development Array: cold H⁺ at 63 MHz towards the Galactic Centre

J. B. R. Oonk^{1,2,3*}, E. L. Alexander^{2,4}, J. W. Broderick², M. Sokolowski^{5,6}, R. Wayth^{5,7}

¹*Leiden Observatory, Leiden University, P.O. Box 9513, NL-2300 RA Leiden, The Netherlands*

²*Netherlands Institute for Radio Astronomy (ASTRON), Oude Hoogeveensedijk 4, 7991 PD Dwingeloo, The Netherlands*

³*SURFsara, P.O. Box 94613, 1090 GP Amsterdam, The Netherlands*

⁴*Jodrell Bank Centre for Astrophysics, School of Physics and Astronomy, The University of Manchester, Manchester M13 9PL, United Kingdom*

⁵*International Centre for Radio Astronomy Research, Curtin University, Bentley, WA 6102, Australia*

⁶*ARC Centre of Excellence for All-sky Astrophysics (CAASTRO), Australia*

⁷*ARC Centre of Excellence for All Sky Astrophysics in 3 Dimensions (ASTRO 3D), Australia*

Accepted 0000. Received 0000; in original form 0000

ABSTRACT

The Engineering Development Array (EDA) is a single test station for Square Kilometre Array (SKA) precursor technology. We have used the EDA to detect low-frequency radio recombination lines (RRLs) from the Galactic Centre region. Low-frequency RRLs are an area of interest for future low-frequency SKA work as these lines provide important information on the physical properties of the cold neutral medium. In this project we investigate the EDA, its bandpass and the radio frequency interference environment for low-frequency spectroscopy. We present line spectra from 30 to 325 MHz for the Galactic Centre region. The decrease in sensitivity for the EDA at the low end of the receiver prevents carbon and hydrogen RRLs to be detected below 40 and 60 MHz respectively. RFI strongly affects frequencies in the range 276–292, 234–270, 131–138, 95–102 and below 33 MHz. Cn α RRLs were detected in absorption for quantum levels $n = 378$ to 550 (39 – 121 MHz) and in emission for $n = 272$ to 306 (228 – 325 MHz). Cn β lines were detected in absorption for $n = 387$ to 696 (39 – 225 MHz). Hn α RRLs were detected in emission for $n = 272$ to 480 (59 – 325 MHz). Hn β lines were detected for $n = 387$ to 453 (141 – 225 MHz). The stacked Hn α detection at 63 MHz is the lowest frequency detection made for hydrogen RRLs and shows that a cold (partially) ionized medium exists along the line of sight to the Galactic Centre region. The size and velocity of this cold H⁺ gas indicates that it is likely associated with the nearby Riegel-Crutcher cloud.

Key words: ISM: clouds – radio lines : ISM – ISM: individual objects: Galactic centre

1 INTRODUCTION

The Square Kilometre Array (SKA) is a next generation telescope with unprecedented sensitivity that is currently under development. This international project consists of two telescope arrays, SKA-Mid (0.3–13.8 GHz) in South Africa and SKA-Low (50–350 MHz) in Australia. The wide variety in science objectives that will be enabled by the SKA have been detailed by the astronomical community in Braun et al. (2015).

A particularly interesting science case for the SKA concerns measuring low-frequency radio recombination

lines (RRL) from hydrogen and carbon and is described in Oonk et al. (2015, and references therein). These weak lines with typical peak optical depths of 10^{-4} to 10^{-3} provide an important method to determine the physical conditions (density n_e and temperature T_e) of cold, diffuse gas that are not easily obtained by other methods (e.g. Oonk et al. 2017, 2015; Salas et al. 2018, 2017; Salgado et al. 2017a,b; Roshi & Kantharia 2011; Gordon & Soroichenko 2009; Kantharia, Anantharamaiah & Payne 1998a; Payne, Anantharamaiah & Erickson 1989). Furthermore, these lines provide a largely unknown foreground signal for measurements of the HI 21 cm line from the epoch of reionization (e.g. Peters et al. 2011; Oonk et al. 2015). SKA-Low in phase 1, also known as SKA1-Low

* E-mail: oonk@astron.nl

(Braun et al. 2015), will provide the necessary 1–2 orders of magnitude increase in surface brightness sensitivity, over existing telescopes such as the Low-Frequency Array (LOFAR, van Haarlem et al. 2013), the Murchison Widefield Array (MWA, Tingay et al. 2013) and the Long Wavelength Array (Ellingson et al. 2013). For our Galaxy this will enable, (i) a full low-frequency Galactic plane RRL survey on arcsec to arcmin scales over a sufficiently wide frequency range to enable detailed modeling of RRL optical depths and line widths, and (ii) detailed measurements of the latitude distribution of low-frequency Galactic RRL emission (Oonk et al. 2015).

The Engineering Development Array (EDA) is a single station SKA1-Low prototype system that is built on the site of the MWA in Western Australia. It is an aperture array comprising 256 dual-polarisation dipoles arranged in a pseudo-random configuration inside a diameter of 35 m. The dipoles are MWA-style bowtie antennas that have modified front-end electronics such that they are sensitive to signals from below 50 MHz to above 300 MHz. Signals from the dipoles are combined via analogue time-delay beamforming to generate a single dual-polarisation beam from the sky. For this experiment, the signals were passed to a GPU-based spectrometer to generate high frequency resolution data, as described in Sect. 2. The full technical specifications are described in Wayth et al. (2017). As SKA1-Low heads towards the critical design review stage in the engineering process, on-site testing and verification is essential. This includes conducting simple science experiments.

Here we report on spectroscopic observations with the EDA aimed at measuring RRLs from hydrogen and carbon. As part of this project we also characterize the spectral line sensitivity, bandpass shape and RFI environment for the EDA.

1.1 Low-frequency RRLs & the Galactic Centre

RRLs are important diagnostics of the physical conditions in the interstellar medium (e.g. Oonk et al. 2017; Gordon & Sorochenko 2009, and references therein). These lines have been observed from hydrogen (HRRL), helium (HeRRL), carbon (CRRL), sulphur (SRRL) and heavier elements (sometimes referred to as XRRL in the literature). There are two types of RRLs that can be distinguished based on their emission process: spontaneous and stimulated. RRLs arising due to spontaneous emission are often associated with discrete sources such as HII regions (e.g. Palmer 1967; Lockman 1976; Pedlar et al. 1978; Roelfsema & Goss 1992; Kantharia, Anantharamaiah & Goss 1998b; Anderson et al. 2011). Here the gas is in local thermal equilibrium (LTE) and it predominantly emits at frequencies above 1 GHz. RRLs arising due to stimulated emission are often associated with diffuse (partially) ionized gas, such as diffuse clouds in the cold neutral medium (CNM). In this case the gas is often found not to be in LTE and it predominantly emits at frequencies below 1 GHz (e.g. Salas et al. 2018; Oonk et al. 2017; Salgado et al. 2017a,b; Payne, Anantharamaiah & Erickson 1989; Konovalenko & Sodin 1980; Shaver 1975).

For our test observation with the EDA we chose to observe the Galactic Centre (GC) region, as it is a bright and

well known source of low-frequency RRL emission and absorption. The GC region has been observed in both HRRL and CRRL over a large range in frequency. Here we will focus on low-frequency (≤ 1.4 GHz) RRLs from in particular hydrogen. The HRRLs measured towards the GC region are observed to be in emission at all frequencies from 141.5 MHz and upwards. Near 1.4 GHz, HRRL have been observed and mapped with 15–30 arcmin resolution using single dish telescopes (e.g. Lockman & Gordon 1973; Lockman 1976; Kesteven & Pedlar 1977; Pedlar et al. 1978; Alves et al. 2015). At this high spatial resolution, the line profile shows signs of multiple components and spans a total velocity range from about -100 km s^{-1} to $+80 \text{ km s}^{-1}$ (e.g. Kesteven & Pedlar 1977).

At lower frequencies, HRRLs have been observed down to 141.5 MHz ($n=359$) (e.g. Roshi & Anantharamaiah 2000, 2001; Roshi, Kantharia & Anantharamaiah 2002; Roshi & Anantharamaiah 1997; Anantharamaiah, Payne & Bhattacharya 1990; Anantharamaiah 1985a,b; Pedlar et al. 1978). These observations have typically been done with large, degree scale beam widths and show that on these scales there is one dominant line component at a local standard of rest (LSR) velocity $v_{\text{LSR}} \sim 0\text{--}10 \text{ km s}^{-1}$, with a full width at half maximum FWHM $\sim 25 \text{ km s}^{-1}$. This component has been referred to as the 0 km s^{-1} component by Pedlar et al. (1978, hereafter P78). P78 also show that the change in line width with spatial resolution is most likely due to beam dilution of the compact regions responsible for the broad line emission. They argue, assuming a single velocity component with a width of 25 km s^{-1} , that the low-frequency HRRL component therefore most likely arises due to stimulated emission from a warm ($T_e \sim 5000\text{--}10000 \text{ K}$), low density ($n_e \sim 1\text{--}30 \text{ cm}^{-3}$), diffuse gas along the line of sight to the GC. Such a gas could exist as part of the warm outer envelopes of HII regions (e.g. Anantharamaiah 1985b). A similar conclusion was reached by Anantharamaiah et al. (1990). Roshi & Anantharamaiah (1997, hereafter R97) present evidence for the possible existence of a narrower, FWHM $\sim 8 \text{ km s}^{-1}$, extended (≥ 1 deg) HRRL component at 328 MHz. Such a narrow line can only arise from a much colder gas with $T_e \leq 1300 \text{ K}$. However, R97 could not confirm this narrow feature as at this frequency it is strongly blended with the FWHM $\sim 25 \text{ km s}^{-1}$ component and they were unable to conclusively reject radio frequency interference (RFI) as a possible origin for this feature.

Carbon RRLs, α ($\Delta n=1$) transitions, towards the GC were detected by Anantharamaiah et al. (1988) near 74 MHz in absorption at a velocity (LSR) of -1 km s^{-1} . This was confirmed by the CRRL Galactic plane survey by Erickson et al. (1995) at 76 MHz. They find extended CRRL absorption and towards the GC these have a peak line-to-continuum ratio of about 10^{-3} , a $v_{\text{LSR}} \sim 0\text{--}5 \text{ km s}^{-1}$ and a FWHM $\sim 24 \text{ km s}^{-1}$. At even lower frequencies, Kantharia & Anantharamaiah (2001) detect CRRL absorption at 34.5 MHz. At higher frequencies, R97 measure extended CRRLs in emission towards the GC at 328 MHz with $v_{\text{LSR}} \sim 0\text{--}7 \text{ km s}^{-1}$ and a FWHM $\sim 20 \text{ km s}^{-1}$. P78 measure CRRL emission at 408 MHz with a line width and velocity similar to that of R97.

2 OBSERVATIONS & DATA REDUCTION

We used the EDA with a drift-scan method to conduct these observations. Scans were taken in 2 minute intervals, with the array being directly centered on the source (GC) in the middle of each scan. During each 2 minute scan no tracking was performed. The telescope beam was re-pointed between scans. The sampling time was 2 seconds (i.e. we obtain 60 individual spectra per scan) and the channel width was 1.25 kHz. In total 262144 channels were observed, providing a bandwidth of 327.68 MHz. To achieve this high spectral resolution over this large bandwidth it was only possible to record data for 1 polarization (the X-polarization) with the EDA GPU-based spectrometer. The bandwidth and frequency range recorded here with the EDA is similar to SKA1-Low, which will have a 300 MHz bandwidth, from 50 to 350 MHz. Originally SKA1-Low planned to have 262144 channels¹ with 1.14 kHz width each, but this has recently been reduced to 65536 channels² with 4.58 kHz width each³.

The details of the EDA observation are summarized in Table 1. The data were obtained in the form of a dynamic spectrum (i.e. time vs. frequency) and are shown in Fig. 1 (in arbitrary intensity units). Useful data are obtained between 30 and 325 MHz, but RFI is observed to strongly affect frequencies in the ranges 276–292, 234–270, 131–138, 95–102 and below 33 MHz. Over this frequency range the FWHM beamsizes for the EDA varies from 1.5 degrees at 325 MHz to 16.4 degrees at 30 MHz. Absolute flux and bandpass calibration observations were not carried out at the time of the observation and follow-up observations could not be carried out because of activities related to the deployment of the Aperture Array Verification System (Benthem et al. 2017). The absolute flux scale is not important as for RRLs the quantity of interest is optical depth. However, contamination from sidelobe emission may affect our optical depth measurements. At low frequencies the sky temperature dominates the system temperature. On degree scales, the GC region is the brightest source on the sky and using low-frequency continuum maps (Haslam et al. 1982; Dowell et al. 2017) we estimate that any sidelobe contamination is less than 10 percent at any frequency for this EDA observation. Directly comparing our measurements near 145 MHz with Anantharamaiah et al. (1990, hereafter APB90), that have the same beamsizes, shows consistency between the measurements and hence that sidelobe contamination is not significant.

Bandpass calibration is important. The frequency response of the telescope was found to be smooth over

~ 0.16 MHz scales. We therefore performed bandpass corrections using a 3rd order polynomial over 0.16 MHz ranges. This is sufficient for the narrow (FWHM ~ 1 –30 kHz) RRLs observed here. The observed dynamic spectrum shows small jumps in the signal level from scan to scan. This corresponds to the re-pointing of the array. To create a normalized spectrum for each scan, we first average the 60 data points per channel. Masking the expected RRL frequencies, we fit the bandpass across the averaged spectrum of each scan over blocks of 128 channels (0.16 MHz) in width. Following Oonk et al. (2014) we divide the observed scan spectrum by this bandpass and subtract one to create a bandpass corrected spectrum in dimensionless units of $T_{\text{line}}/T_{\text{cont}}$.⁴ Here T_{line} and T_{cont} are the measured line and continuum temperatures respectively. This is repeated for each scan. The final spectrum is then created by averaging the corrected spectra for all scans, see Fig. 2. The EDA does not provide Doppler tracking and hence we apply this correction in our offline data reduction procedures.

3 RESULTS

Ca RRLs were detected in absorption for $n = 378$ to 550 (39–121 MHz) and in emission for $n = 272$ to 318 (204–325 MHz); see Fig. 3 and Table 2. Here n is the quantum number of the line transition. The n value for this emission to absorption transition directly indicates that we are observing cool, diffuse gas associated with the CNM (e.g. Salgado et al. 2017b; Oonk et al. 2017; Payne et al. 1989) and we will discuss this in more detail in Sect. 4. In emission these lines have a narrow line profile with a FWHM of about 17 km s^{-1} , whereas in absorption they have a nearly constant FWHM of about 32 km s^{-1} . This change in FWHM cannot be due to pressure or radiation broadening as these scale with $n^{5,2}$ and $n^{5,8}$ respectively. It is more likely that the change in beam size is responsible for the observed change in line width. For $n \geq 500$ (< 52 MHz) an increase in the FWHM to about 56 km s^{-1} is observed. It is likely that also here the change in beam size is responsible. However, pressure or radiation broadening cannot be ruled out for $n \geq 500$. The line profile shapes themselves will be discussed in more detail in Sect. 3.2. The central velocity of the Ca lines is found to shift slightly from around 6 km s^{-1} to 10 km s^{-1} with increasing n . The integrated optical depth of the lines is rather constant for $n < 318$. For $n > 378$ the optical depth first increases up to $n \sim 510$ before it decreases again.

$\text{C}\beta$ ($\Delta n=2$) RRLs were detected only in absorption for $n=387$ to 696 (39–225 MHz); see Fig. 4 and Table 3. For $n=387$ –500 the $\text{C}\beta$ line widths have a FWHM of about 32 km s^{-1} , in agreement with the corresponding α lines. For $n=520$ –605 the FWHM of the $\text{C}\beta$ lines is only 33 km s^{-1} , almost 10 km s^{-1} less than the corresponding Ca lines at the same n . This difference is likely due to beam dilution as at the same frequency (76 MHz) the Ca lines do have the same width as the $\text{C}\beta$ lines. This would imply that at this frequency at least part, if not most, of the broadening is due to the increased beam sizes. At even higher $n=606$ –696 a

¹ The original SKA1-Low design is described at https://astronomers.skatelescope.org/wp-content/uploads/2016/12/SKA-TEL-SKO-DD-001-1_BaselineDesign1.pdf

² The current SKA1-Low design is described at https://astronomers.skatelescope.org/wp-content/uploads/2015/11/SKA-TEL-SKO-0000007_SKA1_Level_0_Science_RequirementsRev02-part-1-signed.pdf

³ For SKA1-Low up to four zoom windows are foreseen that will allow for better frequency resolution at the expense of covering less bandwidth.

⁴ This dimensionless quantity equals negative optical depth, i.e. $T_{\text{line}}/T_{\text{cont}} = -\tau_{\text{line}}$.

strong increase in line width to a FWHM of 86 km s^{-1} is observed. This increase can be attributed to either pressure or radiation broadening, or due to the change in beam size. The central velocities of the $C\beta$ lines are around 10 km s^{-1} which agrees with the $C\alpha$ lines that are observed in absorption. The integrated optical depth of the $C\beta$ lines is found to steadily increase with n from $n=387$ to 696 .

$H\alpha$ RRLs were detected in emission for $n = 272$ to 480 (59–325 MHz); see Fig. 5 and Table 4. The line width shows a modest increase from about 20 to 30 km s^{-1} over the range $n=272$ – 397 . For $n>435$ the line width decreases sharply to around 12 km s^{-1} and is only marginally resolved with the EDA. This decrease in line width could be caused by beam dilution and we will discuss this in more detail in Sect. 4. The central velocity of the $H\alpha$ lines is found to shift slightly from around 10 km s^{-1} to 14 km s^{-1} with increasing n . The magnitude of this shift is similar to what is found for the $C\alpha$ lines. However, the central velocity of the $H\alpha$ lines is on average 3 – 4 km s^{-1} higher as compared to $C\alpha$ at the same frequencies. The absolute optical depth of the line increases from $n=272$ to 318 , after which it steadily decreases again.

An $H\beta$ RRL was marginally detected at $n\sim 420$; see Fig. 4 and Table 5. To verify this detection we varied the range (within $n=342$ to 453) and the number of lines included in our stacking procedure. For all of our stacks, containing 39–85 lines, a 3 – 4σ feature was found with an integrated optical depth varying between -0.6 and -1.0 Hz. The feature is always observed at the same central velocity of $\sim 10 \text{ km s}^{-1}$ and has a FWHM of about 22 km s^{-1} . This is in good agreement with the $H\alpha$ detections and provides additional evidence that this feature is a real $H\beta$ line.

3.1 RRL α to β ratio

For gas in local thermal equilibrium (LTE) we expect the α to β line optical depth ratio to be 3.6 , when measured at the same frequency (e.g. Walmsley & Hoang-Binh 1974; Shaver 1975; Salgado et al. 2017b). Differences from this value would therefore indicate that the gas is not in LTE.

Our highest signal to noise $C\beta$ $n=520$ – 605 detection covers the frequency range 59.1 – 93.0 MHz. For this frequency range we have stacked the corresponding $C\alpha$ $n=411$ – 480 lines and for it we find an integrated optical depth $\int \tau = 6.87 \pm 0.16$, $v_{\text{LSR}} = 10.1 \pm 0.36$ and $\text{FWHM} = 31.3 \pm 0.8 \text{ km s}^{-1}$. The velocity and FWHM for the α profile match well with those of the β profile. The integrated optical depth ratio $C(411\text{--}480)\alpha/C(520\text{--}605)\beta = 2.1 \pm 0.1$. This is in good agreement with Erickson et al. (1995) who measure the $C(441)\alpha/C(555)\beta = 2.1 \pm 0.2$. This low α to β ratio shows that the CRRL emitting gas is not in LTE.

Our $H\beta$ $n=387$ – 453 detection covers the frequency range 140.6 – 225.3 MHz. For this frequency range we have stacked the corresponding $H\alpha$ $n=307$ – 360 lines and for it we find $\int \tau = 7.11 \pm 0.24$, $v_{\text{LSR}} = 9.38 \pm 0.41 \text{ km s}^{-1}$ and $\text{FWHM} = 25.1 \pm 1.0 \text{ km s}^{-1}$. The velocity and FWHM for the α profile match well with those of the β profile. The integrated optical depth ratio $H(307\text{--}360)\alpha/H(387\text{--}453)\beta$ is 8.9 ± 2.7 . This high α to β ratio shows that the HRRL emitting gas is not in LTE. This is consistent with P78 who argue that the low-frequency HRRL are out of LTE when compared with HRRL models for an optically thin

cloud. At higher frequencies, 1.6 GHz , Shaver (1977) measure $H(159)\alpha/H(200)\beta \sim 4$ which is consistent with LTE. This indicates that the higher frequency ($\geq 1.6 \text{ GHz}$) HRRL emission differs from that at lower frequencies (e.g. P78).

Salgado et al. (2017b) show that the α to β line width ratio, when measured at the same frequency, is a useful quantity to investigate line broadening. For carbon we find that down to about 76 MHz the $C\alpha$ and $C\beta$ line widths agree. This implies that here Doppler broadening dominates. Below this frequency the $C\beta$ lines have an increased line width as compared to the α lines, indicating that at these frequencies pressure and radiation broadening become important. Similar behavior for the CRRL line widths was also found for the cool clouds along the line of sight towards Cassiopeia A (e.g. Oonk et al. 2017; Salas et al. 2017; Kantharia, Anantharamaiah & Payne 1998a; Payne et al. 1989). The hydrogen line width will be discussed in more detail in Sect. 4 but our measurements at 183 MHz imply that at this frequency Doppler broadening still dominates.

3.2 RRL line profiles

The HRRL line profiles can be described by a single Gaussian at all frequencies. This is not true for the CRRL line profiles, which are only fitted well by a single Gaussian above 180 MHz (emission). In the 113 – 170 MHz range, where $C\alpha$ transitions from emission to absorption, we find dual peaked line profiles for both $C\alpha$ and $C\beta$. These dual peaks are offset from the main peak at other frequencies. This can be interpreted as evidence that the observed line profile consists of several distinct components with different physical conditions. Studies by Anantharamaiah & Yusef-Zadeh (1989) and Roshi, Kantharia & Anantharamaiah (2002) also show evidence for multiple velocity components.

At lower frequencies, where the CRRLs are in absorption, the $C\alpha$ line profile starts to show signs of asymmetries and broad, possibly Lorentzian, wings that may be associated with radiation and/or pressure broadening. Given that the CRRL line profile at the spatial resolution of the EDA very likely consists of several distinct physical components we do not attempt to disentangle the observed line profiles here. The $H\alpha$ lines do not show strong evidence for deviations from a Gaussian profile. The largest change observed is the decrease in FWHM from about 25 km s^{-1} to 12 km s^{-1} for $n>435$. This transition happens gradually and is most clearly observed in the $n=411$ – 434 stack. Here a narrow line component at $v_{\text{LSR}} \sim 10 \text{ km s}^{-1}$ starts to dominate and a single Gaussian fit does not fit the peak very well and thus overestimates the FWHM for this stack. Below we will focus on this narrow $\sim 12 \text{ km s}^{-1}$ line profile, as it has important implications for the physical conditions of the associated gas.

3.3 Molecular lines

Tentative molecular line features at frequencies near 115 MHz have been reported by Tremblay et al. (2017). We searched our EDA data for molecular lines, using line lists from the Leiden Lambda (Schöier et al. 2005) and the Splat-alogue⁵ catalogs. In the 30 – 325 MHz range and away from

⁵ <http://www.cv.nrao.edu/php/splat/>

regions of strong RFI we find that the 1σ RMS spectral noise in our data is nearly constant at a level of 3×10^{-4} in units of optical depth. In this frequency range we find no evidence for molecular lines.

In particular we searched for individual lines from NO, OH, C_3H , H_2CO and t-HCOOH, and exclude their presence at a 3σ peak optical depth level of 1×10^{-3} per 1.25 kHz channel. These lines have a multitude of transitions in the frequency range probed by our observations and we can therefore use line stacking to probe deeper. Stacking NO in the range 180–210 MHz we derive a 3σ peak optical depth upperlimit of 2×10^{-4} per 1.25 kHz channel. Similarly, we exclude NO, OH, C_3H , H_2CO and t-HCOOH at a 3σ peak optical depth upperlimit per 1.25 kHz channel of 2×10^{-4} , 4×10^{-4} , 3×10^{-4} , 3×10^{-4} and 5×10^{-4} , in the ranges 45–52 MHz, 87–194 MHz, 50–91 MHz, 45–75 MHz and 40–90 MHz, respectively.

If molecular line emission mainly arises due to spontaneous emission then our non-detections are not surprising as their associated Einstein A coefficients are of the order 10^{-21} to 10^{-15} s^{-1} . Alternatively, if these lines are associated with low filling factor gas, relative to the EDA beam, then such line emission would be strongly diluted and difficult to detect with the EDA.

4 DISCUSSION

With the EDA we have observed $C\alpha$ transitions in the range 39–325 MHz, $C\beta$ in the range 39–225 MHz, $H\alpha$ in the range 59–325 MHz and $H\beta$ near 183 MHz. The wide range over which we detect these RRLs would allow us to fit the detailed RRL models by Salgado et al. (2017a) to obtain the physical conditions of the emitting gas. However, we do not attempt this here given the large variation in spatial resolution with frequency for the EDA. The GC region, being an extended and complicated source, would require detailed aperture corrections to align the measurements at different frequencies. Such aperture corrections cannot be done very accurately with our current data set.

4.1 Carbon RRLs

Comparing our CRRL measurements with previous studies (e.g. P78; R97; Anantharamaiah et al. 1988; Erickson et al. 1995; Kantharia & Anantharamaiah 2001; Salgado et al. 2017b) we find reasonable agreement. Our measurements indicate a typical LSR velocity between 5 and 12 km s^{-1} . This is consistent with R97 and slightly higher than P78. The latter find LSR CRRL velocities in the range -2 to 7 km s^{-1} . The differences in the integrated optical depths, line widths and velocity between the various CRRL investigations can likely be accounted for by the different beam sizes used. The offset in velocity, by about 3 km s^{-1} , between the carbon and hydrogen RRLs indicates that these lines arise in different media or volumes. This velocity offset was also observed by R97.

The CRRL optical depths observed here show a behavior that is consistent with cold, diffuse gas and are similar to those observed for the cool clouds along the line of sight to Cassiopeia A (e.g. Oonk et al. 2017; Salas et al. 2017; Salgado et al. 2017b; Kantharia, Anantharamaiah & Payne

1998a; Payne et al. 1989). This is particularly clear from the emission to absorption transition being between 100 and 200 MHz (Oonk et al. 2017) and also directly shows that the CRRL emission must be stimulated (e.g. Salgado et al. 2017a; Payne et al. 1989, R97). Salgado et al. (2017b) has previously attempted to model the GC region using optical depth and linewidth ratios of $C\alpha$ and $C\beta$ lines. They find that models with $T_e \sim 20$ –60 K and $n_e \sim 0.04$ –0.1 cm^{-3} are consistent with the observations. Our data are in agreement with this.

Having briefly discussed the CRRL measurements we will for the remainder of this study focus on the HRRLs and in particular on their line widths.

4.2 Hydrogen RRLs

Our HRRL measurements overlap with previous work around 145 MHz by APB90, 241 and 328 MHz by P78 and 328 MHz by R97. Comparing with these studies, our measurements are largely consistent in terms of v_{LSR} velocity and FWHM line width. In terms of optical depth our detections are typically lower, except near 145 MHz where we agree with APB90. The APB90 measurements have a similar beam size as the EDA and hence the dominant part of the variations in calculated optical depths by different measurements can therefore be understood in terms of their beam sizes. Our observations with the EDA typically have a larger beam size and measure lower optical depths. This indicates that on degree scales the HRRL emitting gas suffers from beam dilution.

Above 80 MHz, our HRRL detections are consistent with a single velocity component at $v_{\text{LSR}} \sim 10 \text{ km s}^{-1}$ with a FWHM $\sim 25 \text{ km s}^{-1}$. This component has previously been referred to as the 0 km s^{-1} component by P78, but later studies find it to be closer to 10 km s^{-1} (e.g. R97). Between 105 and 325 MHz our optical depths are nearly constant. This supports previous conclusions that this low-frequency component of the HRRL emission is dominated by stimulated emission (e.g. P78; R97). Our $H\beta$ detection at 183 MHz furthermore indicates that the low-frequency HRRL emitting gas is not in LTE (see Sect. 3.1).

4.3 HRRL line width

Our detections with the EDA are the lowest frequency HRRL detections to date. Previously these were the 141.5 ($n=359$) and 148.9 MHz ($n=353$) detections by APB90. Below 80 MHz we find, for the first time, that the HRRL line width decreases from a FWHM of 25 km s^{-1} to only 12 km s^{-1} . Fig 5 shows that this change happens gradually between 190 and 80 MHz. Below 80 MHz the line is only marginally resolved by the EDA and as such we will treat this width as an upper limit. The decrease in line width could be explained by beam dilution if the 25 km s^{-1} line width component is less extended than the 12 km s^{-1} component. This would then be similar to the HRRL line profile at 1.6 GHz that shows a decrease in line width with increasing beam size (P78).

At 73 and 63 MHz, where we observe the narrow 12 km s^{-1} line, our FWHM beam size is 6.7 and 7.8 deg. This is much larger than previous measurements and hence it is

possible that the 25 km s^{-1} line width component is diluted to such an extent that only an even more extended component with a line width of 12 km s^{-1} component remains. Alternatively, it is also possible that the 25 km s^{-1} line width component consists of several, different velocity components of which only a component with a width of 12 km s^{-1} remains observable below 80 MHz. Higher spatial and spectral resolution observations below 100 MHz are necessary to test this.

Evidence for the existence of a narrow HRRL component towards the GC has previously been presented at 328 MHz by R97. In their average spectra, they observe a line profile that is consistent with a blend of a narrow 8 km s^{-1} and a broad 38 km s^{-1} component. They also show that this line profile is extended over at least 1 degree in longitude. Due to difficulties with RFI mitigation, R97 could not conclusively verify this narrow component at 328 MHz. Near 310 MHz, our line profiles are best described by a single component with a width of about 20 km s^{-1} , but our spectra have lower signal to noise than R97.

For our narrow 12 km s^{-1} HRRL line width detections at 63 and 73 MHz we can rule out RFI, as we (i) detect the line in each of the two stacks independently and (ii) observe a gradual transition from a 25 km s^{-1} line width at 190 MHz to 12 km s^{-1} below 80 MHz.

4.4 Cold H^+ at 63 MHz

In previous work, P78 and APB90 favor an interpretation where the origin of the low-frequency 25 km s^{-1} HRRL line width component is warm ($T_e \sim 7000 \text{ K}$), low density ($n_e \sim 5\text{--}10 \text{ cm}^{-3}$) gas from the outer envelopes of HII regions. This interpretation is based on the assumption that the measured line width arises due to a single, homogeneous velocity component. However, in the case that it consists of several, narrower components then the warm models no longer apply. For example, R97 showed that the maximally allowed temperature, considering only Doppler broadening, for their narrow line feature is 1380 K. Similarly narrow ($3\text{--}10 \text{ km s}^{-1}$) HRRL components have been found in detailed studies of cool, diffuse clouds at 226–408 MHz (Oonk et al. 2017; Sorochenko & Smirnov 2010) and in HII regions near 1.4 GHz (e.g. Pankonin et al. 1977; Roelfsema & Goss 1992, and references therein). In the latter case these narrow features are typically blended with much broader ($\sim 60 \text{ km s}^{-1}$) line emission that dominates the total HRRL signal at GHz frequencies.

Our measurements show that a narrow HRRL component exists along the line of sight to the GC and dominates the HRRL signal below 80 MHz. Considering the very large beam sizes involved, this emission must be extended over degree scales to remain detectable. It therefore seems likely that this gas is located relatively close to us. Considering only Doppler broadening we can place an upper limit of 3200 K for the temperature of the HRRL emitting gas. However, contrary to earlier studies our detections are at sufficiently low frequencies that pressure and radiation broadening also need to be considered. This enables us to not only constrain the temperature, but also the maximally allowed product of electron density and temperature for the emitting material. At the same time, the absence of significant line broadening observed here between 74 and 63 MHz implies

that radiation and pressure broadening cannot dominate the overall line width at these frequencies. The strongest constraint on n_e and T_e is then obtained at the lowest frequency, i.e. at 63 MHz ($n=470$).

The long line of sight towards the GC has an integrated surface brightness temperature $T_{\text{R},100} \sim 10000 \text{ K}$ at 100 MHz (e.g. Dowell et al. 2017). Given the likely proximity of the gas we will here assume that it sees only a fraction of this radiation. We will therefore conservatively use a power law with $\lambda^{2.6}$ normalized at 100 MHz through $T_{\text{R},100}=2000 \text{ K}$ to describe the radiation field experienced by the HRRL emitting gas. At 63 MHz this will produce only 1.8 km s^{-1} of broadening and this amount scales linearly with the value of $T_{\text{R},100}$ (e.g. Salgado et al. 2017b; Shaver 1975). Higher $T_{\text{R},100}$ values will lead to even more stringent upper constraints on T_e and n_e , whereas lower $T_{\text{R},100}$ values imply that radiation broadening will have a negligible effect on the line width.

Combining Doppler and radiation broadening with pressure broadening (S17b) we constrain the maximally allowed product of T_e and n_e at 63 MHz ($n=470$). This is shown as the green line in Fig. 6. For $n_e \leq 0.2 \text{ cm}^{-3}$ and $T_e \gtrsim 1000 \text{ K}$ Doppler broadening exceeds pressure broadening and drives the allowed densities down with increasing temperature. The green line is a true upper limit as the HRRL line width at 63 MHz is unresolved with the EDA.

The recent RRL optical depth models of Salgado et al. (2017a) can be used to estimate the H^+ column density associated with our HRRL detection at 63 MHz. For $T_e=10\text{--}150 \text{ K}$ and $n_e=0.01\text{--}0.11 \text{ cm}^{-3}$ a detailed grid was computed by Oonk et al. (2017). For this range we require path lengths of $L_{\text{HII}}=0.5\text{--}50 \text{ pc}$ and column densities $N_{\text{HII}}=2 \times 10^{16}\text{--}2 \times 10^{18} \text{ cm}^{-2}$ to explain the observed optical depth. The largest path lengths are obtained for the lowest densities and highest temperatures. This also implies that temperatures significantly higher than about 1000 K are not valid solutions, as these would have unphysical path lengths. For example, the maximally allowed temperature for $n_e=0.01 \text{ cm}^{-3}$ is $T_e=2500 \text{ K}$ and requires $L_{\text{HII}}=4 \text{ kpc}$ and $N_{\text{HII}}=1 \times 10^{20} \text{ cm}^{-2}$ to explain the optical depth at 63 MHz.

Recently there has been discussion in the literature about the different collision rates used for l -changing transitions (Vrinceanu et al. 2012; Guzman et al. 2016, 2017; Vrinceanu et al. 2017). Here l is angular momentum. In particular it has been shown that the semiclassical derived rates in Vrinceanu et al. (2012, hereafter VOS12) underpredict the corresponding quantum mechanical rates for some l -changing collisions. The S17a models that compute the departure coefficients necessary for calculating the HRRL optical depth use the VOS12 semiclassical rates. We find that the differences in the HRRL departure coefficients computed using the VOS12 rates as compared to the coefficients computed using either the Pengelly & Seaton (1964) or the new Vrinceanu et al. (2019) analytical expressions for the rates are not significant for $n \gtrsim 300$ when considering the physical conditions of interest here. The Pengelly & Seaton (1964) and the Vrinceanu et al. (2019) rates both approximate the quantum mechanical rates well and an indepth comparison is provided in Vrinceanu et al. (2019).

As an example, we find for a homogeneous gas slab with $T_e=40 \text{ K}$ and $n_e=0.1 \text{ cm}^{-3}$ (see Sect. 4.5) that the

product of the departure coefficients ($b_n \times \beta_n \propto \int \tau d\nu$) for $n \gtrsim 300$ calculated with the three different rates agree with each other to within 1 percent. This can be understood as the l -changing collision rates are known to primarily affect low to intermediate n values (e.g. Salgado et al. 2017a; Hummer & Storey 1987). We are therefore confident that the differences in the l -changing collision rates discussed in the recent literature do not affect the results presented here. Furthermore, these rates do not affect the HRRL line width analysis presented in Sect. 4.3.

4.5 Origin of the cold H^+ towards the GC

In the previous section we showed that the narrow line width of the HRRL at 63 MHz can only be explained by a cold (partially) ionized gas. The thermal pressure of such a gas, for $T \sim 10^2$ K with a maximally allowed density $n_e = 0.4 \text{ cm}^{-3}$, is $p \sim n_H \times T = 10^2 \times 0.4 / [n_{H^+} / n_H]$ in units $\text{K} \times \text{cm}^{-3}$. Here $[n_{H^+} / n_H]$ is the hydrogen ionization fraction and we assume that $n_e = n_{H^+}$. Since the product of T_e and n_e is an upper limit, the ionization fraction is also an upper limit. For the above temperature and density we require that $[n_{H^+} / n_H] \leq (2-10) \times 10^{-3}$ to remain within the range of typical pressures ($3 \times 10^3 - 2 \times 10^4 \text{ K} \times \text{cm}^{-3}$) measured in the Galactic ISM (e.g. Oonk et al. 2017; Jenkins & Tripp 2011; Wolfire et al. 2003).

With these conditions the HRRL emitting gas at 63 MHz would originate in the cold neutral medium (CNM), likely arising in the cold partially ionized skins of diffuse clouds in the Galactic disc (e.g. Oonk et al. 2017). Requiring pressure balance with the ISM also rules out an origin for the HRRL emitting gas in either the warm ionized medium (WIM) or the warm neutral medium (WNM), as the associated thermal pressures would be too low.

A prominent, nearby cool cloud along the line of sight to the GC is the Riegel-Crutcher (RC) cloud (Riegel & Crutcher 1972). This cloud is located at a distance of about 125 pc and spans at least 40 degrees in Galactic longitude ($l = +25$ to $l = -15$ deg) and 10 degrees in Galactic latitude ($b = -3$ to $b = +7$ deg). It has been observed in HI absorption (e.g. McClure-Griffiths et al. 2006) and various molecular transitions such as CO and OH (e.g. Oka et al. 1998; Crutcher 1973). The cold, atomic gas in this cloud is estimated to have a temperature of about 40 K, a column density of $N(\text{HI}) = (1-4) \times 10^{20}$ and a total line of sight thickness between 1 and 5 pc. The HI observations show that the RC cloud consists of many thin, ~ 0.1 pc, strands (McClure-Griffiths et al. 2006). This type of sub-structure may be responsible for the velocity offset measured here between HRRL and CRRL.

At $T_e = 40$ K the HRRL line width constrains $n_e \leq 0.6 \text{ cm}^{-3}$. However, the models by Salgado et al. (2017a) require that $n_e \leq 0.1 \text{ cm}^{-3}$ for HRRL to be observed in emission. For this combination we find $L_{\text{HII}} = 1$ pc, $N_{\text{HII}} = 3 \times 10^{17} \text{ cm}^{-2}$, $[n_{H^+} / n_H] \sim 1 \times 10^{-3}$ and $p_{\text{th}} \sim 4000 \text{ K cm}^{-3}$. This path length and pressure are consistent with the HI measurements for the RC cloud. The low-frequency CRRL emission near the GC has previously been attributed to the RC cloud and found to be consistent with the physical conditions estimated for the HI absorbing gas (Roshi & Kantharia 2011; Salgado et al. 2017b).

The temperature and density limits derived here for the

HRRL emission at 63 MHz therefore imply that both the HRRL and CRRL emission could be associated with the RC cloud. In particular they could arise in different layers of the partially ionized envelope of the cloud. This would then be similar to the low-frequency RRL emission observed from the cool clouds along the line of sight to Cassiopeia A (e.g. Oonk et al. 2017; Salas et al. 2018).

A cold, ionized plasma will also contribute to low-frequency continuum absorption via free-free processes (Dowell et al. 2017; Kassim et al. 1995; Israel & Mahoney 1990, 1992). Considering the physical conditions for the RC cloud, the HRRL emission at 63 MHz does not cause significant absorption. However, if the broader, $\text{FWHM} \sim 25 \text{ km s}^{-1}$ HRRL emission is a blend of multiple cold, diffuse (to avoid beam dilution) gas components, then these must have a higher density to avoid detection below 80 MHz and could then account for the observed continuum absorption. Additional detailed broad-band, high spatial and spectral resolution observations with e.g. LOFAR, MWA and the future SKA1-Low, are necessary to further investigate this.

4.6 Future SKA1-Low observations

The scientific importance of sensitive, low-frequency RRL surveys to probe the diffuse CNM, with the future SKA1-Low, was outlined in Oonk et al. (2015). There we focused on how CRRL, in combination with HRRL and HI 21 cm measurements, allow us to derive important physical properties of the diffuse CNM that are not easily obtained via other methods. In particular we showed how the thermal pressure, carbon abundance, warm to cold fraction of the HI 21 cm signal and the hydrogen ionization rate can be obtained, and specific examples were given for the GC region and the Magellanic Clouds.

In Oonk et al. (2017) and Salas et al. (2018) we showed that low-frequency CRRLs trace cool, diffuse clouds in the CNM and we found that the physical conditions of CRRL emitting gas are consistent with CO-dark gas. This would, potentially, make the CRRLs an important probe of CO-dark gas. Low-frequency HRRLs appear to be related to the corresponding CRRLs and their characteristics show that they must also arise in cool, partially ionized gas (this work). However, we find that the HRRLs do not match the CRRLs exactly, in either the derived physical conditions (Oonk et al. 2017) or in velocity space (this work). To make progress in understanding the low-frequency HRRL emitting gas we require the following: (i) better spatial resolution to map its morphology and relate it to other known gas phases, and (ii) more sensitive, high spectral resolution, wide-band observations to derive its physical conditions.

The future SKA1-Low can meet these requirements and will enable us to determine the thermal balance, chemical enrichment, and ionization rate of the cold, diffuse medium from degree scales down to scales corresponding to individual clouds and filaments in our Galaxy. Table 1 in Oonk et al. (2015) provides 5σ peak optical depth limits for observing extended RRL emission with SKA1-Low when using the core array (2 km effective baseline) with 1 kHz

channels and stacking the lines in groups of 9.⁶ The corresponding column density limits for observing low-frequency HRRL emitting gas with SKA1-Low can then be calculated for a given set of physical conditions. As an example we will here use a homogenous gas slab, observed along the line of sight to the GC, with physical conditions similar to those discussed for the RC cloud in Sect. 4.5, i.e. $T_e=40$ K, $n_e=0.1$ cm⁻³, $T_{R,100}=2000$ K and FWHM=12 km s⁻¹. Invoking the S17a models and Table 1 in Oonk et al. (2015), SKA1-Low will be able to detect H⁺ column densities in the range $(4-20)\times 10^{15}$ cm⁻² at the 5σ line peak level and with an angular resolution between 1.5 and 8.6 arcmin. At the distance of the RC cloud this angular resolution corresponds to sub-pc scale spatial resolution. Considering hydrogen ionization fractions of 10^{-4} to 10^{-3} this corresponds to a neutral gas column density of about 10^{19} to 10^{20} cm⁻².

The sensitivity of SKA1-Low for RRLs decreases at the high-frequency end of the band and below 110 MHz. The latter is due to a steep drop-off in the bandpass below 110 MHz. Towards the higher frequencies it is a combination of a slow bandpass drop-off and a decreasing Galactic background radiation field. Broadband sensitivity is very important to capture the distinctive features of RRL models, e.g. the emission to absorption transition and maximum emission turnover (Oonk et al. 2017). However, currently the biggest issue for observing low-frequency RRLs from cool, diffuse gas with SKA1-Low is the recently planned decrease in the numbers of channels from 262144 to 65536. As shown here, and in Oonk et al. (2017, 2015), these low-frequency RRL observations require a channel width of at most 1 kHz to obtain the minimally necessary velocity resolution, i.e. 2 to 12 km s⁻¹ across the 50–350 MHz range. The reduction in the number of channels for SKA1-Low therefore has important consequences for RRL measurements in that the available bandwidth is effectively reduced from 300 MHz to 4 zoom windows covering 16 MHz each. This setup would then allow for only 21 % of the available RRLs to be observed instantaneously and thus a factor 5 loss in observing time. Furthermore, to clearly resolve the HRRL lines, as observed here, even higher spectral resolution would be necessary at the lowest frequencies.

5 CONCLUSIONS

We have presented 0–328 MHz spectroscopic observations with the EDA towards the GC region. Useful data were obtained in 30–325 MHz range. We find that about 10 percent of our data is affected by RFI. This percentage can be lowered by observing with higher spectral resolution, as shown by LOFAR (e.g. Oonk et al. 2017; Salas et al. 2017). The antenna response, as reflected in the bandpass for the EDA, shows the expected decrease in sensitivity below 60 MHz and above 180 MHz.

With the EDA we have detected CRRLs between 39 and 325 MHz and HRRLs between 59 and 325 MHz respectively towards the GC region. For the HRRLs our observations

are the first detection of this line below 145 MHz and reveal a previously unknown cold, diffuse, ionized gas component. We summarize our main conclusions below.

- The peak HRRL emission is located at LSR velocities +10 to +15 km s⁻¹, and is located at a velocity 3–4 km s⁻¹ higher than CRRL over the entire frequency range. Both HRRL and CRRL shift by about 5 km s⁻¹, towards higher LSR velocities, with decreasing frequency and increasing beam size.
- The slowly varying optical depth of HRRL and the emission to absorption transition of CRRL show that the RRL emitting gas towards the GC is dominated by stimulated emission.
- The α to β line ratios for both HRRL and CRRL imply that the low-frequency RRL emitting gas is not in LTE.
- The EDA CRRL measurements are consistent with previous work by E95, R97, and S17b showing that the CRRL emission most likely originates in cool, diffuse cloud emission that is part of the CNM.
- Below 80 MHz we find a decrease in HRRL line width from a FWHM of 25 km s⁻¹ to ≤ 12 km s⁻¹. This decrease, in combination with the large beam size, reveals that a cold, diffuse H⁺ gas exists on degree scales towards the GC region and dominates at the lowest frequencies.
- The optical depth of the cold, narrow (FWHM=12 km s⁻¹) H⁺ emission at 63 MHz does not cause significant free-free absorption. The broader 25 km s⁻¹ component, if cold, would be able to explain the observed continuum absorption at low frequencies.

The narrow, weak nature of the HRRL emission observed below 80 MHz explains why it has been difficult to measure these lines in the past. These HRRLs are likely part of the same CNM component as the CRRL, albeit that they do not arise in exactly the same volume. The presence of low-frequency HRRL and CRRL associated with cold, diffuse gas is consistent with recent models (e.g. Salgado et al. 2017a). A possible origin for the RRL emission observed here is the nearby RC cloud, as its proximity, size and the background radiation field create a particularly favorable situation for detection with the EDA.

Future observations with SKA1-Low will enable us to determine the morphology and physical conditions of the low-frequency HRRL emitting gas discovered here. However, improved broadband sensitivity with (sub-)kHz spectral resolution is desirable in order for SKA1-Low to efficiently observe these low-frequency RRLs over large scales in the Galaxy. If achieved, this would enable detailed RRL modeling constraining the physical conditions of the media in which they arise on arcsec to arcmin scales (e.g. Oonk et al. 2017, 2015; Salas et al. 2018, 2017; Salgado et al. 2017a).

ACKNOWLEDGMENTS

J.B.R.O. acknowledges financial support from NWO Top LOFAR-CRRL project, project No. 614.001.351. E.L.A.

⁶ Please note that the numbers in Oonk et al. (2015) refer to an early version of the SKA1-Low design. The design for SKA1-Low has not been finalized and as such the detailed sensitivity across the frequency band is not yet known.

would like to thank the ASTRON/JIVE summer student programme for a fellowship in 2017. This scientific work makes use of the Murchison Radioastronomy Observatory, operated by CSIRO. We acknowledge the Wajarri Yamatji people as the traditional owners of the Observatory site.

REFERENCES

- Alves M. I. R., Calabretta M., Davies R. D., Dickinson C., et al., 2015, *MNRAS*, 450, 2025
- Anderson L. D., Bania T. M., Balser, D. S., Rood R. T., et al., 2011, *ApJS*, 194, 32
- Anantharamaiah, K. R. 1985a, *JApA*, 6, 177
- Anantharamaiah, K. R. 1985b, *JApA*, 6, 203
- Anantharamaiah K. R., Payne H. E, Erickson W. C., 1988, *MNRAS*, 235, 151
- Anantharamaiah K. R., Yusef-Zadeh F., 1989, *IAUS*, 136, 159
- Anantharamaiah K. R., Payne H. E, Bhattacharya D., et al., 1990, in M.A. Gordon and R.L. Sorochenko (eds.), *Radio Recombination Lines: 25 Years of Investigation*, 259-265, Kluwer Academic Publishers
- Anantharamaiah K. R., Erickson W. C., Payne H. E, et al., 1994, *ApJ*, 430, 682
- Benthem P., Gerbers M., Bij de Vaate J. G., Wynholds ., et al.; , 2017, XXXII General Assembly and Scientific Symposium of the International Union of Radio Science (URSI GASS)
- Braun R., Bourke T. L., Green J. A., Keane E. F., et al., 2015, *Advancing Astrophysics with the Square Kilometre Array*, 2 vols., Dolman Scott Ltd., Thatcham, UK, 2015.
- Crutcher R. M., 1973, *ApJ*, 185, 857
- Dowell J., Taylor G. B., Schinzel F. K., Kassim N. E., Stovall K., 2017, *MNRAS*, 469, 4537
- Ellingson S. W., Taylor G. B., Craig J., et al., 2013, *ITAP*, 61, 2540
- Erickson W. C., McConnell D., Anantharamaiah K. R., 1995, *ApJ*, 430, 682
- Gordon M. A., Sorochenko R. L., 2009, *Radio Recombination Lines: Their Physics and Astronomical Applications* (Springer Scienc+Business Media)
- Guzman F., Badnell N. R., Williams R. J. R., van Hoof P. A. M., Chatzikos M., Ferland G. J. 2016 *MNRAS* 459, 3498
- Guzman F., Badnell N. R., Williams R. J. R., van Hoof P. A. M., Chatzikos M., Ferland G. J. 2016 *MNRAS* 464, 312
- Israel F. P., Mahoney M. J., 1992, *A&A*, 261, 47
- Israel F. P., Mahoney M. J., 1990, *ApJ*, 352, 30
- Jenkins E. B., Tripp T. M., 2011, *ApJ*, 734, 65
- Haslam C. G. T., Salter C. J., Stoffel H., Wilson W. E., 1982, *A&AS*, 47, 1
- Hummer, D.G., Storey P.J. 1987, *MNRAS* 224, 801
- Kantharia N. G., Anantharamaiah K. R., Payne H. E., 1998, *ApJ*, 506, 758
- Kantharia N. G., Anantharamaiah K. R., Goss W. M., 1998, *ApJ*, 504, 375
- Kantharia N. G., Anantharamaiah K. R., 2001, *JApA*, 22, 51
- Kassim N. E., Perley R. A., Dwarakanath K. S., Erickson W. C., 1995, *ApJ*, 455L, 59
- Kesteven M. J., Pedlar, A., 1977, *MNRAS*, 180, 731
- Konovaleenko A. A., Sodin L. G., 1980, *Nature*, 283, 360
- Lockman F. J., Gordon M. A., 1973, *ApJ*, 182, 25
- Lockman F. J., 1976, *ApJ*, 209, 429
- McClure-Griffiths N. M., Dickey J. M., Gaensler B. M., Green A. J., Haverkorn M., *ApJ* 652, 1339
- Oka T., Hasegawa T., Hayashi M., Handa T., Sakamoto S., 1998, *ApJ*, 493 730
- Oonk J. B. R., van Weeren R. J., Salgado F., et al., 2014, *MNRAS*, 437, 3506
- Oonk J. B. R., Morabito L. K., Salgado F., Toribio M. C., et al., 2015, *Proceedings of Advancing Astrophysics with the Square Kilometre Array (AASKA14)*, 139
- Oonk J.B. R., van Weeren R. J., Salas P., Salgado F., et al., 2017, *MNRAS*, 465, 1066
- Palmer P., 1967, *ApJ*, 149, 715
- Pankonin V., Walmsley C. M., Wilson T. L., Thomasson P., 1977, *A&A*, 57, 341
- Payne H. E., Anantharamaiah K. R., Erickson W. C., 1989, *ApJ*, 341, 890
- Pedlar A., Davies R. D., Hart L., Shaver P. A., 1978, *MNRAS*, 182, 473
- Pengelly R. M., Seaton M. J. 1964, *MNRAS*, 127, 165
- Peters W. M., Lazio T. J. W., Clarke T. E., Erickson W. C., Kassim, N. E., 2011, *A&A*, 525, 128
- Riegel K. W., Crutcher R. M., *A&A*, 18, 55
- Roelfsema P. R., Goss W. M., *A&ARv*, 4, 161
- Roshi A. D., Anantharamaiah K. R., 1997, *MNRAS*, 292, 63
- Roshi A. D., Anantharamaiah K. R., 2000, *ApJ*, 535, 231
- Roshi A. D., Anantharamaiah K. R., 2001, *ApJ*, 558, 226
- Roshi A. D., Kantharia N. G., Anantharamaiah K. R., 2002, *A&A*, 391, 1097
- Roshi A. D., Kantharia N. G., 2011, *MNRAS*, 414, 519
- Salas P., Oonk J.B. R., van Weeren R. J., Salgado F., et al., 2017, *MNRAS*, 467, 2274
- Salas P., Oonk J.B. R., van Weeren R. J., Wolfire M. G., et al., 2018, *MNRAS*, 475, 2496
- Salgado F., Morabito L. K., Oonk J. B. R., et al., 2017a, *ApJ*, 837, 141
- Salgado F., Morabito L. K., Oonk J. B. R., et al., 2017b, *ApJ*, 837, 142
- Schöier F. L., van der Tak F. F. S., van Dishoeck E. F., Black J. H., 2005, *A&A* 432, 369
- Shaver P. A., 1975, *Pramana*, 5, 1
- Shaver P. A., 1977, *A&A*, 59L, 31
- Sorochenko R. L., Smirnov G. T., 2010, *ARep*, 54, 776
- Tingay S. J., Goeke R., Bowman J. D., et al., 2013, *PASA*, 30, 7
- Tremblay C. D., Hurley-Walker N., Cunningham M., et al., 2017, *MNRAS*, 471, 4144
- van Haarlem M. P., Wise, M. W., Gunst, A. W., et al., 2013, *A&A*, 556, A2
- Vrinceanu D., Onofrio R., Sadeghpour H. R., 2012, *ApJ*, 747, 56
- Vrinceanu D., Onofrio R., Sadeghpour H. R., 2017, *ApJ*, 471, 3051
- Vrinceanu D., Onofrio R., Oonk J.B. R., Salas P., Sadeghpour H. R., 2019, *ApJ*, submitted
- Walmsley M., Hoang-Binh D., 1974, *MmSAI*, 45, 171
- Wayth R., Sokolowski M., Booler T., Crosse B., et al., 2017, *PASA*, 34, 34

Wolfire M. G., McKee C. F., Hollenbach D., Tielens A. G.
G. M., 2003, ApJ, 587, 278

Parameter	EDA
Field center RA (J2000)	17h45m40s
Field center DEC (J2000)	-29d00m28s
Observing date	13-07-2017
Observing start (UT)	14:54:53
Observing end (UT)	18:15:10
Total on-source time	03h20min
Frequency range	0–327.68 MHz
Number of channels	262144
Channel width	1.25 kHz

Table 1. Details of the EDA observation. For the frequency range please note that only the range 30–325 MHz provides useful data. Over the 30–325 MHz range the spatial resolution changes from 1.5 to 16.4 deg and the spectral resolution changes from 2.3 to 25 km s⁻¹

C α transition	Frequency	FWHM _{beam}	$\int \tau d\nu$	v_{LSR}	FWHM _{line}
n -range (#lines)	[MHz]	[deg]	[Hz]	[km s ⁻¹]	[km s ⁻¹]
272–281 (8)	310.1	1.6	-2.82 ± 0.78	5.4 ± 2.4	17.4 ± 5.6
288–289 (2)	272.6	1.8	≤ 2.24	—	[20]
302–305 (4)	234.2	2.1	≤ 1.11	5.7 ± 1.3	[20]
306–318 (13)	216.1	2.3	-2.61 ± 0.53	6.2 ± 1.7	17.2 ± 4.0
319–333 (15)	189.6	2.6	≤ 0.47	—	[20]
334–341 (8)	170.5	2.9	≤ 0.32	—	[20]
343–360 (18)	151.4	3.2	≤ 0.21	—	[30]
378–397 (20)	113.0	4.3	5.27 ± 0.40	7.3 ± 1.4	38.3 ± 3.4
411–434 (24)	87.3	5.6	5.96 ± 0.33	10.5 ± 0.8	30.5 ± 2.0
435–460 (26)	73.5	6.7	7.36 ± 0.25	9.6 ± 0.5	32.3 ± 1.2
461–480 (20)	63.1	7.8	6.89 ± 0.24	10.7 ± 0.5	30.9 ± 1.2
481–500 (20)	55.7	8.8	6.54 ± 0.31	11.7 ± 0.7	29.1 ± 1.6
501–520 (20)	49.4	9.9	7.93 ± 0.36	10.9 ± 1.0	44.7 ± 2.4
521–540 (20)	44.0	11.2	5.51 ± 0.29	7.8 ± 1.1	42.4 ± 2.6
541–550 (10)	40.4	12.2	6.14 ± 0.52	5.4 ± 3.0	$56.5 \pm ???$

Table 2. Cn α stacked RRL measurements. The integrated line optical depth $\int \tau d\nu$, local standard of rest velocity v_{LSR} and full width at half maximum line width FWHM_{line} are obtained from single Gaussian fits to the observed line profiles; see Fig. 3. The line optical depth τ is defined as $-T_{\text{line}}/T_{\text{cont}}$, with T_{line} the line temperature and T_{cont} the continuum temperature. The first column shows the quantum range considered and the values in the parentheses provide the number of lines stacked. The upper limits for non-detections are given in units of optical depth at the 3σ level and are integrated over the expected line width that is given in square brackets in the FWHM column.

C β transition	Frequency	FWHM _{beam}	$\int \tau d\nu$	v_{LSR}	FWHM _{line}
n -range (#lines)	[MHz]	[deg]	[Hz]	[km s ⁻¹]	[km s ⁻¹]
342–354 (13)	310.1	1.6	≤ 0.48	—	—
387–453 (67)	183.0	2.7	2.64 ± 0.32	9.8 ± 1.8	30.8 ± 4.3
476–500 (25)	112.9	4.3	2.83 ± 0.31	9.7 ± 1.6	28.7 ± 3.7
520–605 (86)	76.1	6.5	3.32 ± 0.13	10.6 ± 0.6	33.7 ± 1.5
606–696 (91)	48.8	10.1	4.19 ± 0.25	9.1 ± 2.5	85.6 ± 5.9

Table 3. Cn β stacked RRL measurements. The $\int \tau d\nu$, v_{LSR} and FWHM_{line} are obtained from single Gaussian fits to the observed line profiles. See Fig. 4 and Table 2 for more information.

H α transition (bin)	Frequency	FWHM _{beam}	$\int \tau d\nu$	v_{LSR}	FWHM _{line}
<i>n</i> -range (#lines)	[MHz]	[deg]	[Hz]	[km s ⁻¹]	[km s ⁻¹]
272–281 (8)	309.9	1.6	-5.39 ± 0.84	9.6 ± 0.7	19.4 ± 3.5
288–289 (2)	272.4	1.8	-8.24 ± 1.71	15.8 ± 2.1	20.4 ± 4.9
302–305 (4)	234.1	2.1	-8.02 ± 1.32	6.7 ± 1.6	19.5 ± 3.7
306–318 (13)	216.0	2.3	-8.75 ± 0.54	10.2 ± 0.7	23.8 ± 1.7
319–333 (15)	189.5	2.6	-7.81 ± 0.59	9.4 ± 1.0	26.8 ± 2.3
334–341 (8)	170.4	2.9	-6.61 ± 0.47	11.6 ± 0.8	24.2 ± 2.0
343–360 (18)	151.3	3.2	-5.68 ± 0.40	8.1 ± 0.9	24.8 ± 2.0
378–397 (20)	113.0	4.3	-3.67 ± 0.40	9.2 ± 1.5	29.3 ± 3.7
411–434 (24)	87.3	5.6	-2.61 ± 0.33	12.2 ± 2.6	41.6 ± 6.1
435–460 (26)	73.5	6.7	-0.98 ± 0.16	12.9 ± 0.9	11.5 ± 2.2
461–480 (20)	63.1	7.8	-0.56 ± 0.15	15.8 ± 1.6	11.9 ± 3.7
481–500 (20)	55.7	8.8	≤ 0.056	—	[12.0]

Table 4. H α stacked RRL measurements. The $\int \tau d\nu$, v_{LSR} and FWHM_{line} are obtained from single Gaussian fits to the observed line profiles. See Fig. 5 and Table 2 for more information.

H β transition	Frequency	FWHM _{beam}	$\int \tau d\nu$	v_{LSR}	FWHM _{line}
<i>n</i> -range (#lines)	[MHz]	[deg]	[Hz]	[km s ⁻¹]	[km s ⁻¹]
342–354 (13)	310.0	1.6	≤ 0.51	—	[20]
387–453 (67)	182.9	2.7	0.80 ± 0.24	159.7 ± 3.2	22.4 ± 7.6
476–500 (25)	112.9	4.3	≤ 0.14	—	[20]
520–605 (86)	76.1	6.5	≤ 0.056	—	[20]
606–696 (91)	48.8	10.1	≤ 0.046	—	[12]

Table 5. H β stacked RRL measurements. The $\int \tau d\nu$, v_{LSR} and FWHM_{line} are obtained from single Gaussian fits to the observed line profiles. See Fig. 4 and Table 2 for more information.

This paper has been typeset from a \TeX / \LaTeX file prepared by the author.

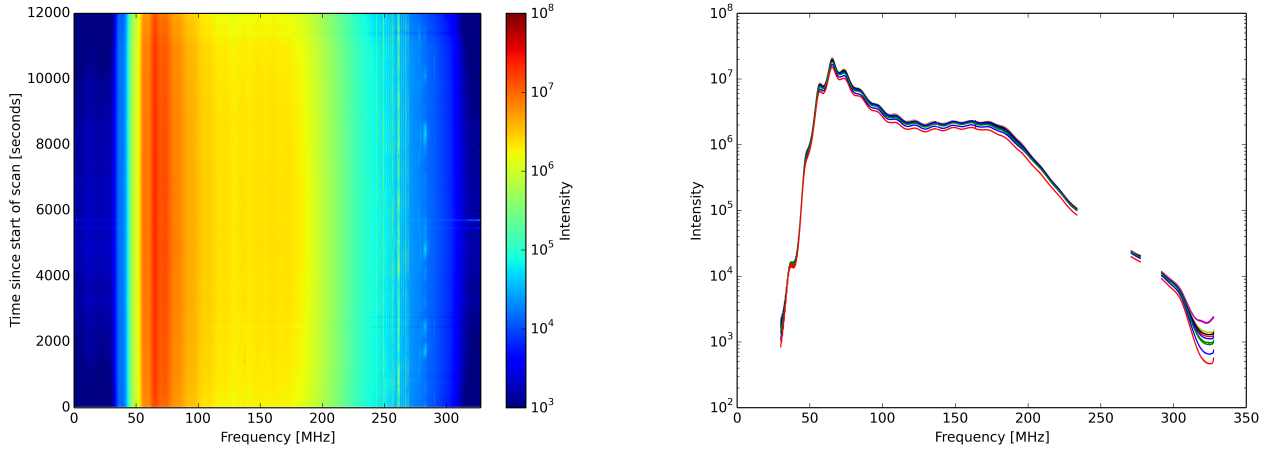


Figure 1. EDA observation of the GC region. (Left) Observed data shown as frequency (horizontal axis) vs. time (vertical axis). (Right) Bandpass shown as the average power in arbitrary units (A.U.) vs. frequency for each 20 min scan. Different colors represent different scans and show the stability of the bandpass profile over time.

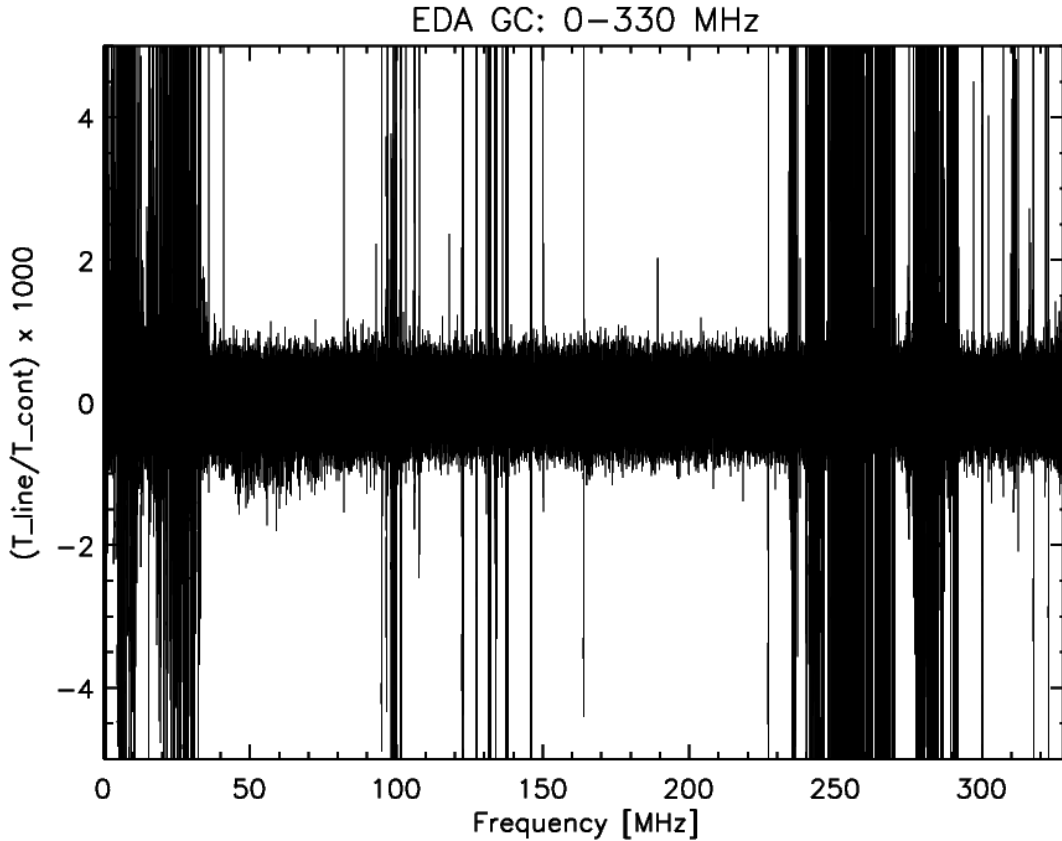


Figure 2. EDA observed (time averaged) spectrum towards the GC region in units of $(T_{\text{line}}/T_{\text{cont}}) \times 1000$, with T_{line} the line temperature and T_{cont} the continuum temperature. Note that in the range from 40–90 MHz the carbon RRLs are directly visible in absorption at $(T_{\text{line}}/T_{\text{cont}}) \times 1000$ around -1. The signal spikes with an absolute value of $(T_{\text{line}}/T_{\text{cont}}) \times 1000$ larger than about 2 are all associated with strong RFI. In the 30–325 MHz range and away from regions with strong RFI the 1σ RMS noise level is reasonably constant around 3×10^{-4} , per 1.25 kHz channel, in units of $T_{\text{line}}/T_{\text{cont}}$.

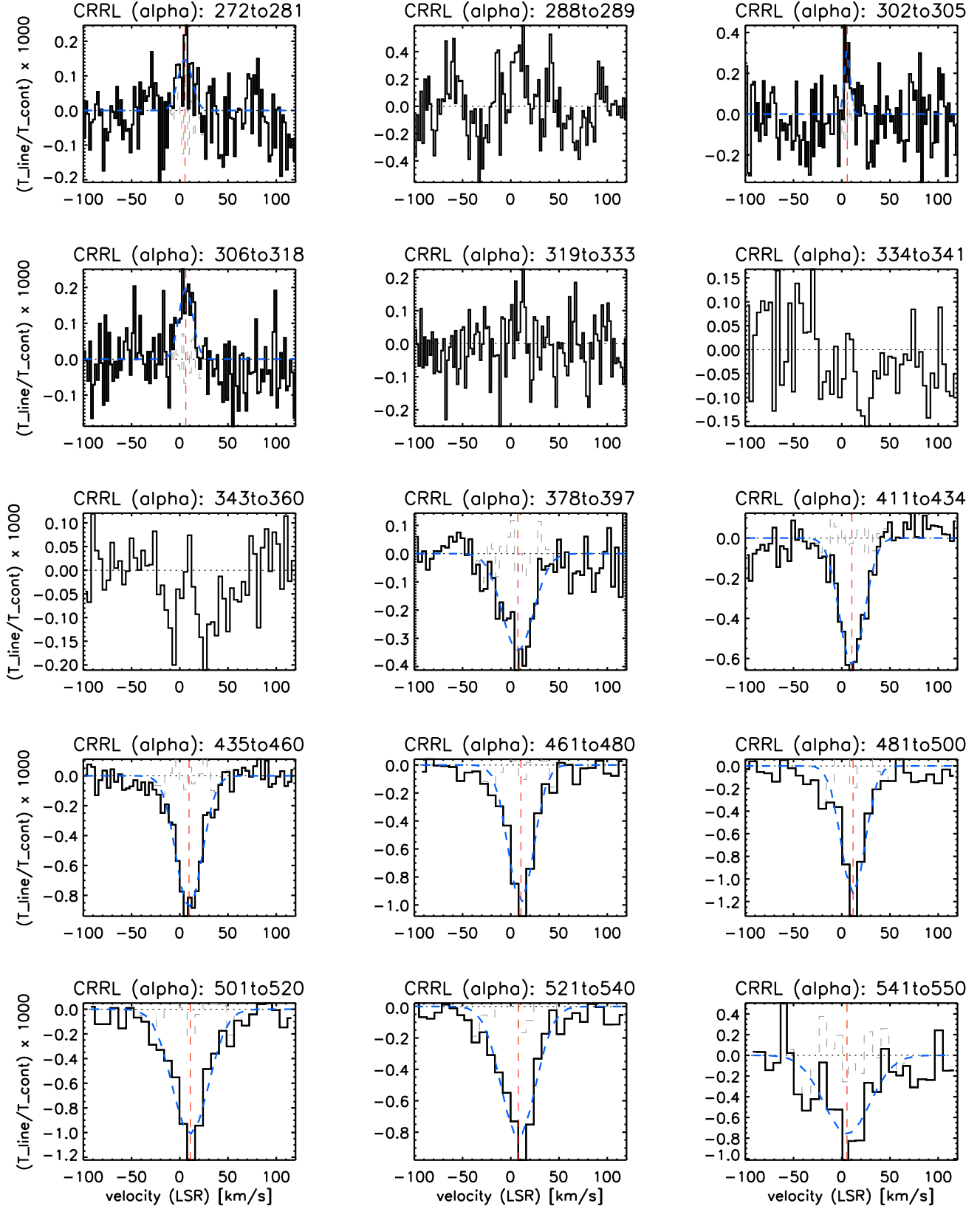


Figure 3. $Cn\alpha$ stacked RRL spectra for different n -ranges. The thick dashed (blue) line shows the Gaussian fit. The dark, thin dashed (red) line shows the fitted line centroid and the light, thin dashed (grey) line shows the fit residuals. The x-axis and y-axis labels are same for all panels.

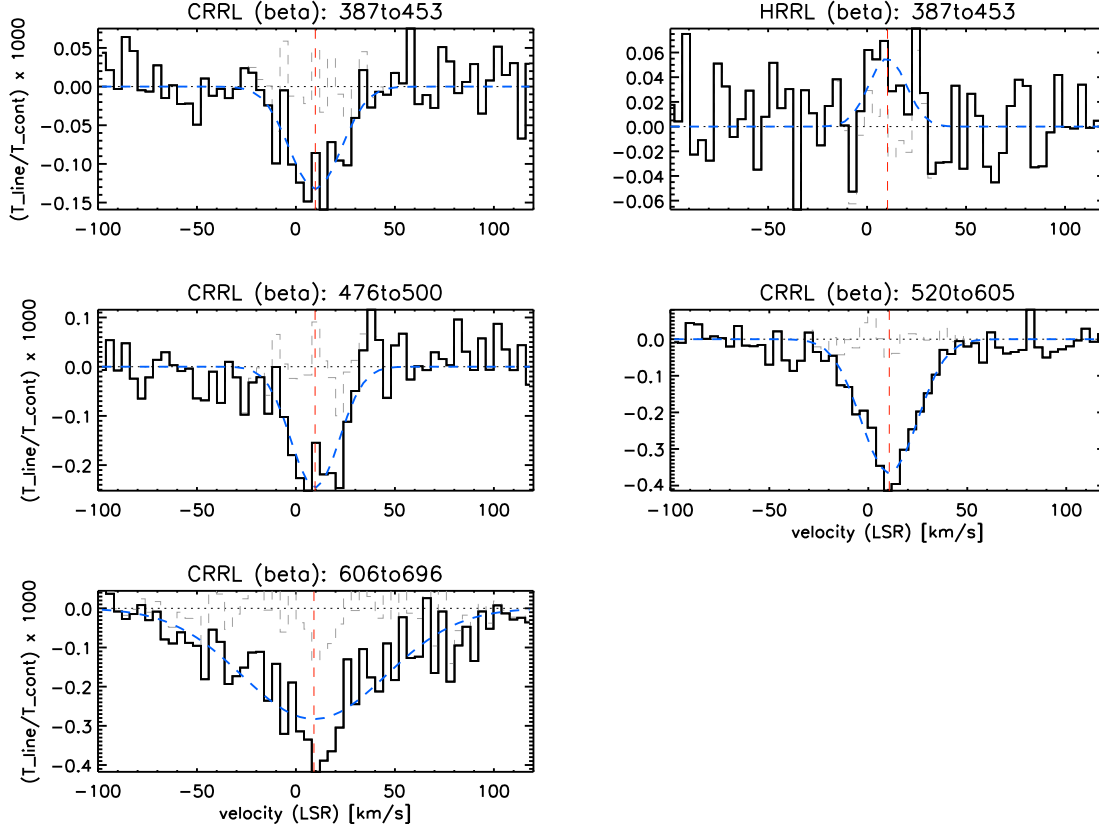


Figure 4. $Cn\beta$ and $Hn\beta$ stacked RRL spectra. For $Hn\beta$ we have only one detection and show it in the upper right corner for direct comparison with the corresponding $Cn\beta$ stack in the upper left corner. The middle and lower panels show $Cn\beta$ detection at lower frequencies. The thick dashed (blue) line shows the Gaussian fit. The dark, thin dashed (red) line shows the fitted line centroid and the light, thin dashed (grey) line shows the fit residuals. The x-axis and y-axis labels are same for all panels.

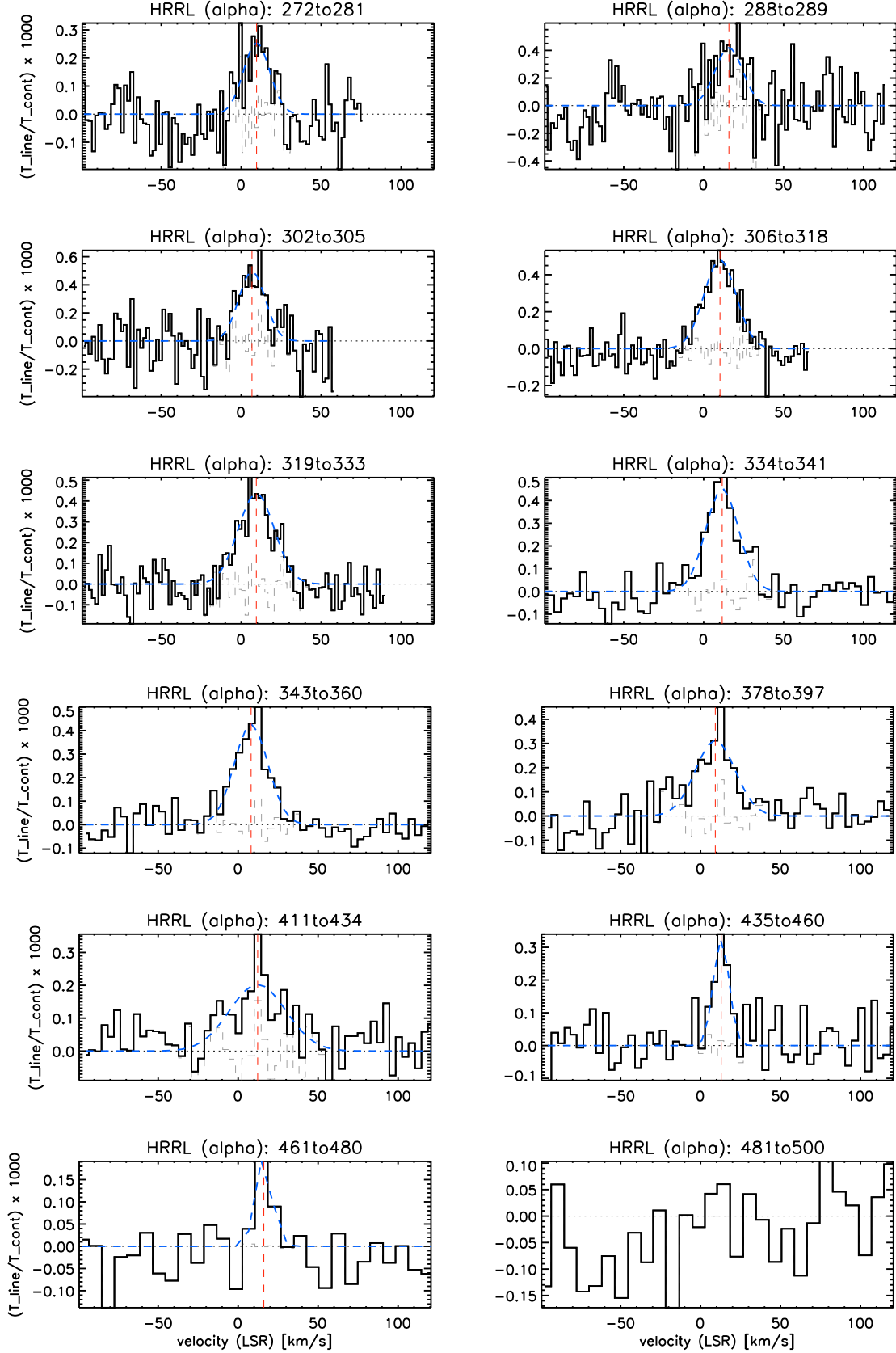


Figure 5. $H_n\alpha$ stacked RRL spectra for different n -ranges. The thick dashed (blue) line shows the Gaussian fit. The dark, thin dashed (red) line shows the fitted line centroid and the light, thin dashed (grey) line shows the fit residuals. The x-axis and y-axis labels are same for all panels. For $n \geq 481$ (≤ 59 MHz) we have tried stacking $H_n\alpha$ over a variety of n -ranges, but do not detect HRRL's. As an example of these non-detections we have shown here the $n=481$ -500 line stack.

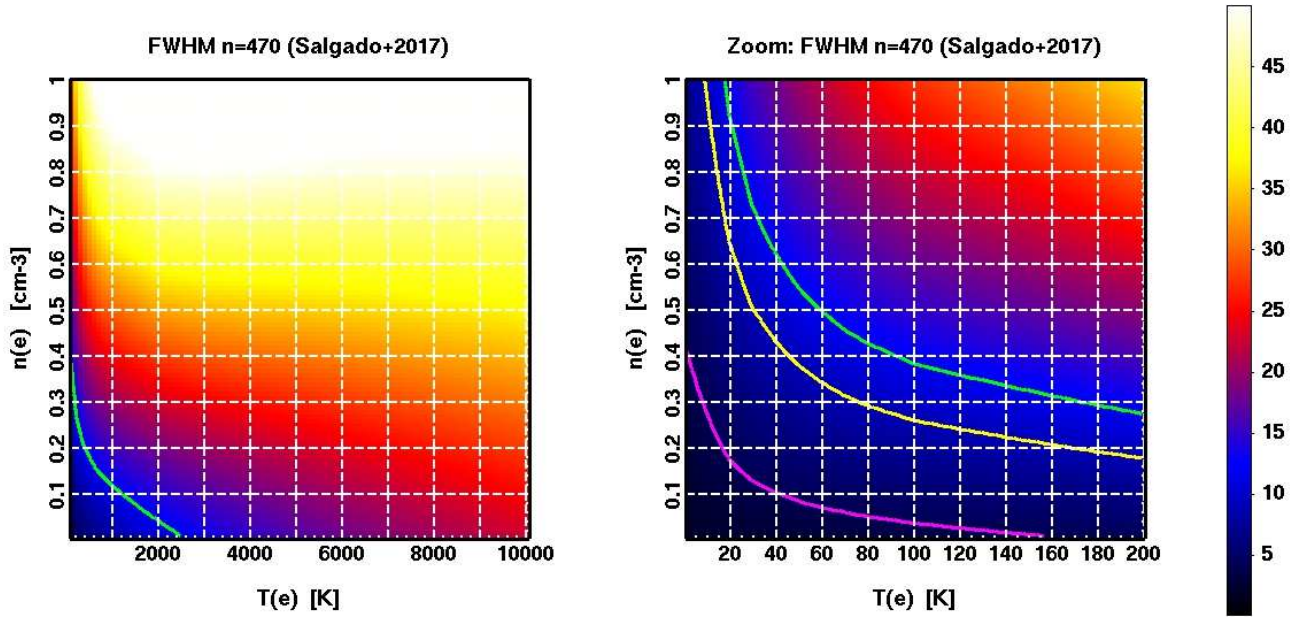


Figure 6. Line broadening (color scale) in units of km s^{-1} as a function of gas temperature T_e and density n_e for a fixed Galactic, power-law ($\beta=2.6$) radiation field normalized at 100 MHz by $T_{R,100}=2000$ K. We consider Doppler, pressure and radiation broadening here following Salgado et al. (2017b). (Left) Showing the line width for the full grid in T_e and n_e . Here the solid green line shows the maximally allowed combination of pressure and temperature for the HRRL line width of 12 km s^{-1} at 63 MHz ($n=470$). (Right) A zoom-in on the low temperature (0–200 K) part of the grid. The green (top) solid line is the same as in the left panel. The yellow (middle) and magenta (bottom) lines show the corresponding T_e , n_e limits for line widths of 9 and 4 km s^{-1} respectively.